ACS APPLIED MATERIALS & INTERFACES

Research Article

www.acsami.org

Gold Nanoisland Films as Reproducible SERS Substrates for Highly Sensitive Detection of Fungicides

Boris N. Khlebtsov,[†,‡] Vitaly A. Khanadeev,[†,‡] Elizaveta V. Panfilova,[†] Daniil N. Bratashov,[‡] and Nikolai G. Khlebtsov*[,†,‡]

[†]Institute of Biochemistry and Physiology of Plants and Microorganisms, Russian Academy of Sciences, 13 Prospekt Entuziastov, Saratov 410049, Russia

[‡]Saratov State University, 83 Ulitsa Astrakhanskaya, Saratov 410012, Russia

Supporting Information

ABSTRACT: A wet-chemical approach is used to fabricate centimeter-scale gold nanoisland films (NIFs) with tunable morphology of islands and with strong electromagnetic coupling between them. The approach consists in a uniform seeding of small gold nanoparticles on a glass or silicon substrate, followed by controllable growth of the seeds into small nanoislands. A special technique for TEM sampling was developed to follow the gradual formation of larger-sized isolated nanoparticles, nanoislands of sintered overgrown seeds, and a complete gold layer with nanoscale cracks. The electromagnetic field distribution inside the fabricated NIFs was calculated by FDTD simulations applied to actual TEM images of the fabricated samples rather than to artificial models commonly used. SERS measurements with 1,4-aminothiophenol (ATP) molecules demonstrated the analytical enhancement factor about of 10^7 and the fundamental enhancement factor about of 10^8 for optimized substrates. These values were at least 1 order of magnitude higher than that for self-assembled arrays of gold nanostars and silver nanocubes. SERS spectra of independent samples demonstrated good sample-to-sample reproducibility in terms of the relative standard deviation (RSD) of the main peaks less than 20%. Additionally, Raman maps with 1 μm increment in $X-Y$ directions of NIFs (800 spectral spots) demonstrated good point-to-point repeatability in the intensity of the main Raman vibration modes (RSD varied from 5% to 15% for 50 randomly selected points). A real-life application of the fabricated SERS substrates is exemplified by the detection of the thiram fungicide in apple peels within the 5−250 ppb linear detection range. Specifically, the NIF-based SERS technology detected thiram on apple peel down to level of 5 ng/cm^2.

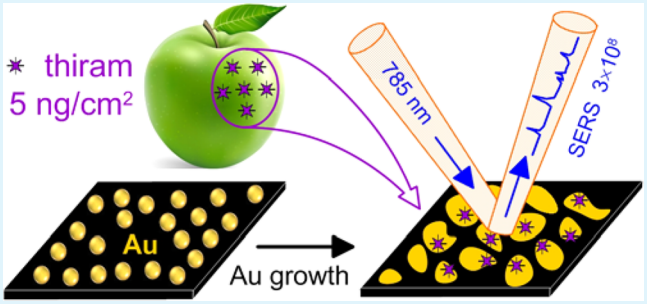

KEYWORDS: *SERS, nanoisland films, gold nanostars, silver nanocubes, thiram, pesticides*

INTRODUCTION

Raman spectroscopy has found various analytical applications, especially in research fields requiring high analyte specificity because of the close relation between the Stokes shifts and the molecular structure of reporters. As the Raman scattering cross-section is typically too low for direct measurements,[1] the discovery of surface-enhanced Raman scattering (SERS)[2] was crucial for practical applications. Owing to the electromagnetic field enhancement associated with "hotspots" on a rough metal surface[3] (normally referred to as SERS substrates[4]), the local magnitudes of the fundamental SERS enhancement factor (EF)[5] can reach 10^{11}, whereas the surface-averaged values are usually about 10^8 in the best experiments.[6,7]

The fabrication techniques for SERS substrates can be divided into two main classes. The first includes top-down approaches, in which a metal layer is controllably deposited on a parent rough or nanoscale arranged surface. Well-known examples are SERS substrates fabricated by use of nanosphere lithography,[8] lithographic patterning,[9] or "film-over-spheres" platforms.[10] The second consists in the bottom-up formation of metal nanoparticle (NP) aggregates or self-assembled NP structures. Thanks to the recent progress in metal NP synthesis, the published examples of bottom-up SERS substrates include assemblies made of noble metal nanospheres,[1,11] nanorods,[12−15] nanostars,[16−18] mesoflowers,[19] and other NP types. For improving the reproducibility of self-assembling processes, parent microstructures such as micron-sized pillars,[20] elastomeric templates,[21,22] and colloidal silica crystals[23,24] have been proposed. However, those attempts have resulted in the process of fabrication becoming overly complex.

Regardless of the fabrication method employed, the effective SERS substrate should meet the following criteria:[25] high fundamental and analytical EFs,[5,7] point-to-point repeatability and sample-to-sample reproducibility, stability on storage,

Received: November 26, 2014
Accepted: March 12, 2015
Published: March 12, 2015

DOI: 10.1021/acsami.5b01652
ACS Appl. Mater. Interfaces 2015, 7, 6518−6529

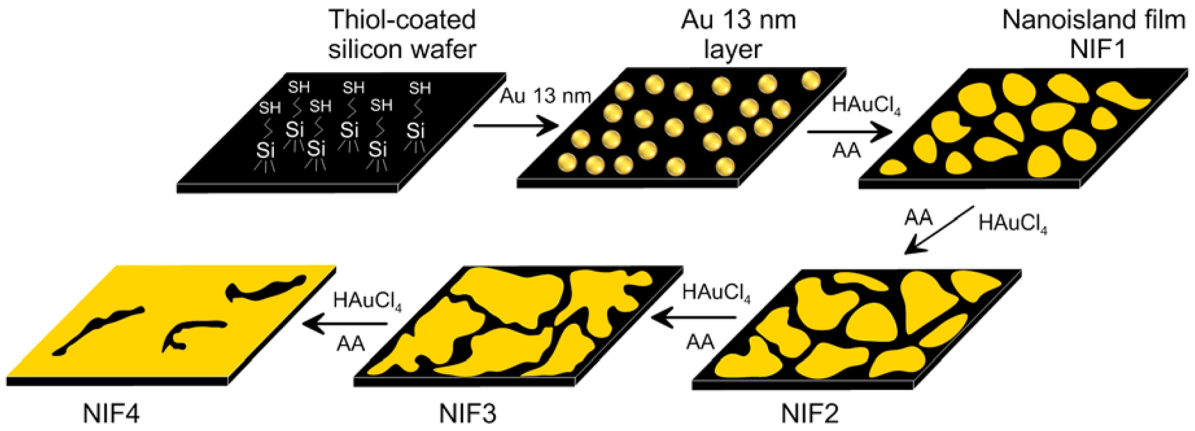

Figure 1. Schematic illustration of the basic steps in fabricating gold NIFs through four sequential overgrowth steps (designated NIF1, NIF2, NIF3, and NIF4, respectively).

applicability to different analytes, and low cost. Although numerous SERS substrates have been described in the literature, only few have been subjected to these criteria.

Semicontinuous metal island films, prepared by electron-beam evaporation, are promising SERS substrates[26] with high EFs and good reproducibility.[27,28] In this Research Article, we show that gold nanoisland films (NIFs) can be obtained by a very simple and low-cost two-step wet-chemical protocol. In the first step, small (13−15 nm) gold NPs are seeded on a glass or silicon thiol-coated surface. The second step involves a standard reduction of $HAuCl_4$ by ascorbic acid (AA) to overgrow the seeds into small nanoislands.

In general, the basic idea behind seed-mediated overgrowth approach is not new. For example, a similar approach has been reported to produce silver[29,30] NP arrays. Furthermore, Oyama and co-workers[31,32] described two variants of seed-mediated overgrowth techniques to form gold nanoparticle arrays on an indium tin oxide (ITO) surface. However, all previous studies reported the formation of overgrown NP arrays rather than formation of NIFs. As a result, the morphology of gold NP arrays reported in refs 31−33 is completely different from the morphology of NIFs obtained in this work. To the best of our knowledge, a pure wet-chemical approach has not been used previously to fabricate gold NIFs similar to those fabricated through top−down approach.[26] To access the mechanistic description of NIFs, we developed a special technique for TEM sampling to follow the gradual formation of larger-sized isolated nanoparticles, nanoislands of sintered overgrown seeds, and a complete gold layer with nanoscale cracks. In contrast to common practice of FDTD simulations with artificial models resembling actual samples, here we use the actual TEM images to simulate the electromagnetic field distribution and electromagnetic coupling between NIF nanostructures. In addition to being simple to make, the obtained NIF substrates demonstrated excellent point-to-point repeatability and sample-to-sample reproducibility of SERS responses with an average fundamental and analytical EFs[5,7] of about 10^8 and 10^7, respectively.

Another important point that we address here is the sensitive SERS detection of fungicides in fruits. Rapid, simple, and sensitive detection of pesticides has attracted much interest recently.[34,35] From this point of view, SERS seems very promising due to the fingerprint nature of SERS spectra, low spectrum accumulation time, and accessibility of cheap and portable Raman devices. But many pesticides usually have very small Raman cross sections and a low affinity for gold or silver surfaces. For example, in the first pesticide study, Alak and Vo-Dinh[36] demonstrated that an accidentally spilled pesticide can be detected in soil samples only when present at a high concentration (1.25% by weight). More recent studies have focused on the development of SERS substrates and their testing with simple pesticide solutions,[37−41] but only few were aimed at real-life detection. For example, Shende et al.[42] conducted rapid SERS detection of 50 ppb of chlorpyrifos methyl artificially added to orange juice. The overall time of analysis was about 12 min, including the time taken by solvent and solid-phase extraction. In this article, the prepared NIFs are shown to be suitable for fast (5 min) SERS detection of ppb concentrations of the thiram fungicide both in model solutions and in thiram-treated apples. The NIF-based SERS technology detected thiram on apple peel down to level of 5 ng/cm^2, which is almost one order lower than that reported previously.[41]

RESULTS AND DISCUSSION

Fabrication and Characterization of Gold NIFs. We employed a seed-mediated growth process to prepare gold NIFs as highly active SERS substrates. The NIFs were obtained through a two-step procedure shown schematically in Figure 1. First, 13 nm gold seeds were attached to the surface of thiolated glass or silicon wafers. In the second step, the seeds were allowed to grow into nanoislands (NIs) in the presence of additional $HAuCl_4$ and AA as a reductant. Actually, the second step can involve several sequential overgrowth steps. Typically, we used four overgrowth steps, producing NIFs designated NIF1, NIF2, NIF3, and NIF4, respectively.

Thirteen-nm gold NP layers were fabricated on microscopic coverslips or silicon wafers by alternate immersion into cross-linker and colloidal gold solutions.[43] Note that the successful functionalization of glass by silane-thiol linkers can be monitored during the washing steps by the "lotus leaf" effect[44] on a hydrophobic glass. The process of NP deposition yielded a uniformly decorated surface with a disordered array of 13 nm gold NPs, as shown in Figure S1 (Supporting Information). As the uniform coverage of the substrate surface by gold seeds is a key point in the formation of final NIFs, we applied a multistep control for NP deposition. First, the ratio between the functionalized surface area and the total number of 13 nm NPs added was kept constant in all experiments: 2 cm^2 of the substrate area were immersed in 3 mL of colloid with a number concentration of 6×10^{12} particles/mL. Second, the incubation

DOI: 10.1021/acsami.5b01652
ACS Appl. Mater. Interfaces 2015, 7, 6518−6529

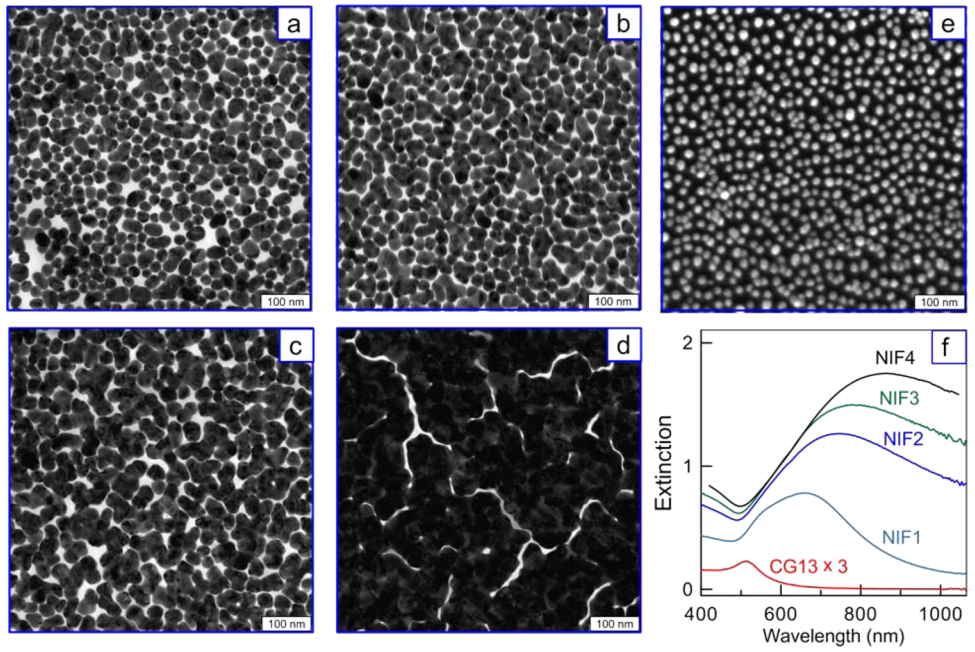

Figure 2. TEM images of NIF1 (a), NIF2 (b), NIF3 (c), and NIF4 (d) obtained by four overgrowth steps for the parent 13 nm seeds (e). The scale bars are 100 nm. (f) Extinction spectra of NIF1−NIF4 and the parent 13 nm gold NP layer (designated CG13 × 3; the spectrum was multiplied by 3 for convenient comparison). All samples were obtained with glass coverslips.

time was 3 h. A shorter incubation time led to decreased surface coverage and to less uniform deposition of NPs, whereas a longer incubation time resulted in the formation of irregular NP aggregates. From a practical point of view, the seeding of NPs on a glass surface can easily be monitored by visual inspection of the glass color. After 15 min incubation, the coverslip became slightly red-colored owing to plasmonic extinction of the adsorbed NPs near 520 nm. During the deposition time of about 3 h, the red color gradually deepened. After 3 h, the surface density of the adsorbed NPs was about 37%, as estimated from the extinction spectra of colloidal gold NPs (see Figure S2, Supporting Information and comments therein). When the incubation time was extended further, purple and blue spots appeared in the central part of the coverslip, that are indicative of NP aggregation and plasmon coupling between closely packed NPs. The absence of NP aggregation on the glass surface was additionally confirmed by measuring the extinction spectra of the coverslips. Succeeding experiments used only those coverslips that had a slightly broadened absorbance peak near 520 nm (Figure S3, Supporting Information).

Metal NIFs were formed by immersing the seeded coverslips or silicon wafers in growth solutions containing $HAuCl_4$, $AgNO_3$, and the reductant AA (see Methods). The amount of additionally deposited gold can be controlled with a tunable relationship between the Au concentration and the total surface of the parent substrate. In our protocol, we immersed a 2 cm^2 coverslip in 3 mL of 120−720 μM $HAuCl_4$. If lower concentrations are used, the seeded NPs tend to grow with a quasispherical shape around the initial seeds, without notable changes in the color, extinction spectra, and SERS responses of the substrates. Thus, concentrations of $HAuCl_4$ lower than 100 μM were not sufficient to form SERS-active NIFs under our experimental conditions. On the other hand, as the metal concentration in the growth solution approaches 720 μM, some of the seeded NPs start to overgrow together into small nanoisland (NI) structures. Further increase in the gold concentration or volume of the growth solution yielded large gold microstars on the NIF surface (Figure S4, Supporting Information). It is evident that the formation of microstars is also an unwanted process, as it will affect the uniformity of the final NIFs. To increase the final surface density of NIs while keeping their uniformity, we repeated the overgrowth procedure for additional three times under optimal overgrowth conditions (see Methods). No starlike structures or strongly disordered islands were observed for the sequentially overgrown samples.

Figure 2 shows TEM images of four NIFs (NIF1−NIF4, panels a−d, respectively) obtained by four sequential overgrowth steps for the initial 13 nm seeds shown in panel (e). The corresponding SEM images of the NIFs are shown in Figures S5 and S6 (Supporting Information).

In the first step, the initial, almost spherical NP seeds transformed into more irregular quasispherical or elongated particles (about 70%) with a small portion of sintered NPs (about 30% of islands formed from two to three NPs). After the second step, a typical NI contained three to five NPs and about 90% of all gold was included in the NI structures (Figure 2b). After the third step, the gaps between the NIs decreased further and only few isolated nanoparticles could be seen (Figure 2c). Finally, the fourth step gave rise to an almost complete gold layer with rare nanoscale cracks. It is evident that the additional growth of NIs resulted in greater surface density of gold from step to step. The gold surface density can roughly be derived from binarized TEM images (Figure S7, Supporting Information) as the ratio between black and white pixels. For example, the average surface density of NIF1 was about 80%. Thus, even the first overgrowth step led to a dramatic increase in surface coverage from 37% of the initial seeds to 80% of NIF1. Therefore, one would expect that after the second overgrowth step, the substrates would be filled almost completely. Surprisingly enough, the surface density increased

DOI: 10.1021/acsami.5b01652
ACS Appl. Mater. Interfaces 2015, 7, 6518−6529

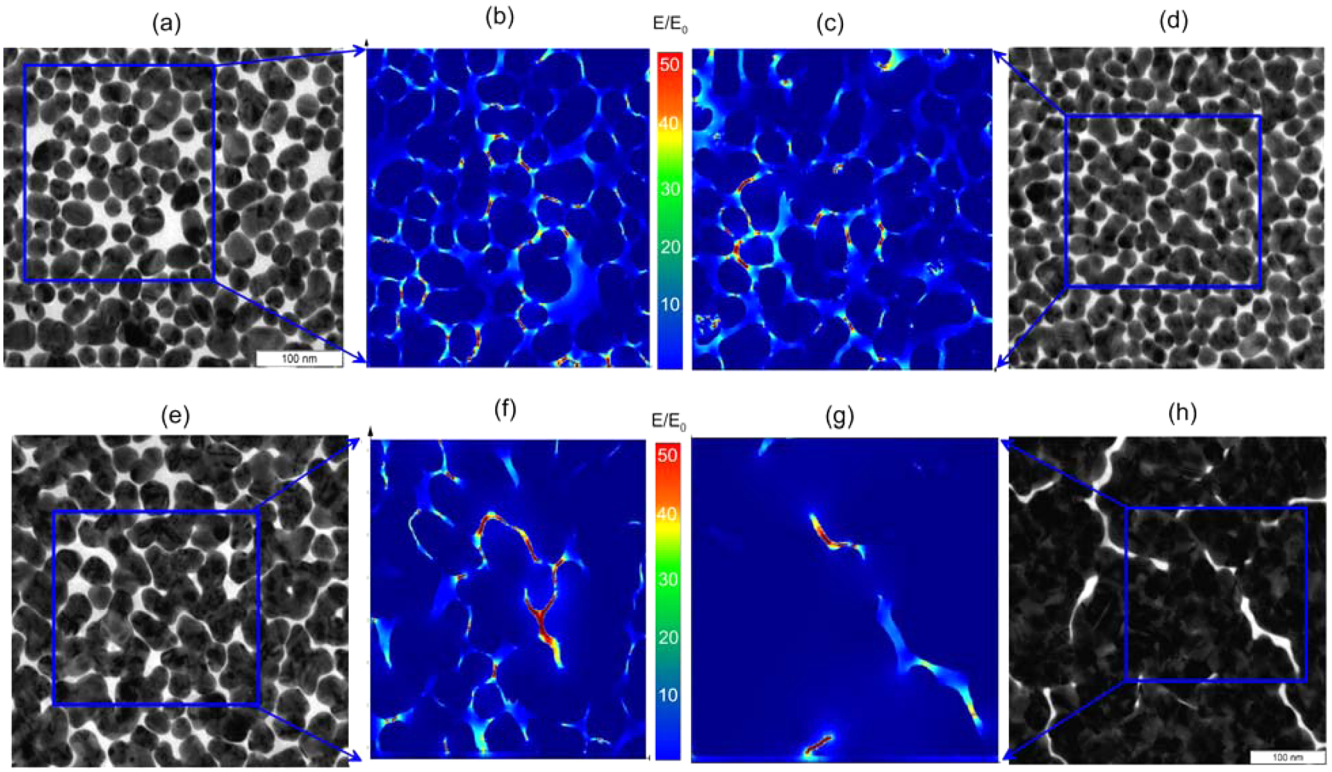

Figure 3. TEM images of NIF1 (a), NIF2 (d), NIF3 (e), and NIF4 (h). The simulation areas are shown by blue squares. Panels b, c, f, and g show the calculated field distributions inside the films under 785 nm excitation.

only weakly, from 80% to 83% and 87% and 96% after the second, third, and fourth steps, respectively. Since no NPs were observed in the growth solution, we believe that the weak increase in the size of NIs was accompanied by an increase in their thickness. It is this "vertical" growth process that can explain the quite moderate increase in the surface density after the first overgrowth step. For example, the thickness of the NIF4 layer was 50 ± 12 nm, as measured by SEM at an angle of 45° (Figure S8, Supporting Information). Clearly, the thickness of the initial seeds was increased by almost four times (from 13 to 50 nm).

The optical properties of the NIFs changed strongly after each overgrowth step. These changes were evident by naked eye inspection of the samples' colors and from measurements of their extinction spectra (Figure 2f). The first overgrowth step gave rise to a light blue color and shifted the plasmon resonance peak from 520 nm (13 nm isolated seeds) to 670 nm for NIF1. In the next three steps, the color of the samples changed to deep blue, green, and golden-yellow, indicating the formation of an almost complete gold layer.

The observed changes in the extinction spectra can be qualitatively explained with using multiparticle Mie model.[45] The gradual increase in the NP size and their surface density lead to the increase in the total area occupied by NPs and to the gradual increase of the NIF extinction caused by increased absorption and far-field scattering of the incident light. On the other hand, the NP sintering lead to narrower interparticle gaps and to the more effective plasmonic coupling between densely packed NPs and NIs. This behavior is similar to that observed previously[45] for lattice and randomly distributed gold nanoparticles with increased surface density. Both, the multiparticle Mie model and the T-matrix cluster simulations[45] predicted a gradual shift of the plasmonic peak position because of the increased size of interacting NPs and decreased interparticle separations. In our case, the collective plasmonic peak shifts from 670 (NIF1) to 850 nm (NIF4). It should be emphasized, however, that for large particles possessing both the quadrupole and the dipole single-particle peaks, the electromagnetic interaction in densely packed arrays can result in quite different effect: suppression of dipole absorption band and dominating of only quadrupole band in the coupled array spectra.[46]

FDTD Modeling of Electromagnetic Field Distribution. Nanoscale gaps between metal nanostructures are the primary features needed to produce the highest possible enhancement in Raman scattering.[47] As the local electric field E_{loc} decays as R^{-3} and the fundamental EF is roughly proportional[5] to $|E_{loc}|^4$, close proximity of molecules to a hot spot is essential for high enhancement of Raman response. To determine the approximate gain in SERS intensity enhancement caused by the nanoscale gaps in the NIFs, we performed extensive 3D FDTD simulations of field distribution in our NIFs under 785 nm plane-wave excitation. By contrast to many routine FDTD simulations for simplified artificial nanostructures, we used actual TEM images (similar to those shown in Figures 2 and 4) to build adequate geometrical models for irregular NIFs. This produced TEM-based 2D maps, whereas the film thickness was chosen to be 30 nm for all simulations. Such an approach to using actual TEM-based images rather than some artificial models is similar to that reported previously for evaporated gold NIFs.[26]

Figure 3 shows the TEM-based structures employed in our calculations, together with the obtained distributions of the local field intensity. These simulations show that the maximal field enhancement was about 200 in several "hottest" points within the simulated area. Taking into account the fourth power enhancement law, we expect the maximal electro-

DOI: 10.1021/acsami.5b01652
ACS Appl. Mater. Interfaces 2015, 7, 6518−6529

magnetic contribution to the total (electromagnetic + chemical) EF to be about 1.6×10^9. Of course, because of the small percentage of hot spots, the average EF value should be at least several times lower. It is also clear, that FDTD estimation of EF does not include any chemical contribution. The highest Raman signal enhancement can also be observed experimentally only when the Raman active molecules are located precisely in a hot spot of a NIF.

For Raman molecules with a high affinity for the gold surface, one could expect a uniform coverage of the substrate. In this case, in close proximity to the substrate surface (e.g., when the distance is shorter than 0.5 nm), the integral field enhancement can serve as a key parameter to characterize substrate efficiency. Figure S9 (Supporting Information) shows an example of field distribution calculated in this 0.5 nm plane.

In general, the observed variations between NIFs sensitivity and reproducibility are related with evident changes in NIF morphology, packing density of sintering particles, etc. All these changes lead to variations in the spatial density of electromagnetic hot spots and, eventually, to variations in the NIF enhancing properties.

Qualitatively, the observed changes in FDTD simulations can be explained by using simplest two-particle dipole-interacting model. Restricting our consideration to the near-field zone, we can write the coupled dipole field E_{coup} as[48]

$$E_{coup} = \frac{\alpha}{2\pi d^3} \frac{E_0}{1 - \left(\frac{\alpha}{2\pi}\right)} \quad (1)$$

where the incident field E_0 is directed along the particle axis ("in-phase" mode), α is the polarizability of each dimer particle, and d is the interparticle distance. Of course, this consideration is too simplified and does not take into account the local field effects, strong inhomogeneity of the electric field between particles, where the multipole description is actually needed.[49] Nevertheless, for increased (grown) particles and for decreased interparticle separation, eq 1 predicts enhanced near-field caused by the dipole−dipole interaction, because α scales as the particle volume and the inteparticle separations decrease with growing of the initial seeds and their gradual sintering.

Sensitivity and SERS Enhancement Measured with 1,4-Aminothiophenol. To evaluate the sensitivity of fabricated NIFs, we employed ATP solutions as described previously by Zhou et al.[40] Specifically, the gained SERS spectra were measured for a series of diluted ATP solutions from 10^{-10} to 10^{-7} M (Figure 4). The measurements were performed after application of a 1 μL of ATP solution with concentrations ranging from 10^{-10} to 10^{-7} M. Typically, the applied solution formed a dried spot (~15 mm^2) during several seconds.

For minimal ATP concentrations, 10^{-10} M and 10^{-9} M, the SERS peaks cannot be resolved, except for small irregular peaks for the 10^{-9} M. Therefore, the detection limit of NIF2 and NIF3 substrates can be roughly estimated as 10^{-8} M, whereas the detection limits of assembled silver cubes and gold nanostars were essentially lower by one or two orders (data not shown). In general, NIF2 films demonstrated better SERS performance as compared to NIF3 and NIF4 samples. In our opinion, NIF2 samples demonstrated the best SERS efficiency owing to an optimal spatial distribution of grown islands and separations, which ensure an optimal surface density of electromagnetic hot spots. It should also be noted that our detection limit, 10^{-8} M, is one order lower than that reported by Zhou et al.[40] Besides differences in substrates themselves, a possible reason for smaller SERS efficiency can be related to different measurement conditions, including different excitation wavelength (663 nm),[40] laser spots and power, nonuniform adsorption of APT molecules on SERS substrates, etc.

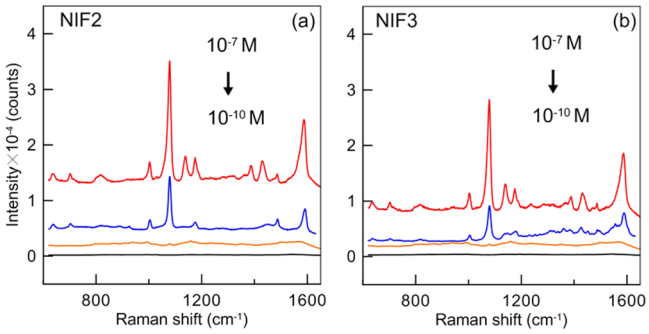

Figure 4. SERS spectra of different concentrations of ATP solution collected with NIF2 (a) and NIF3 (b) films. All spectra were corrected to the background baseline and averaged for randomly chosen 10 points. The measurements were performed with a Renishaw inVia confocal Raman microscope.

To examine the experimental SERS properties of the different NIFs, SERS spectra were acquired from an analyte (in our case, 1,4-aminothiophenol, ATP) adsorbed on substrates by immersion in 100 μM ATP solutions (Figure 5b−e). This molecular probe was selected because of its well-documented properties, including the low chemical (charge-transfer) contribution to the amplified Raman intensities of ATP.[50] The normal Raman spectrum of ATP served as the benchmark data (Figure 5a). Additionally, self-assembled silver nanocubes and gold nanostars were used as control SERS substrates. TEM and SEM images of those nanoparticles and self-assembled substrates are shown in Figures 5g−j. SERS spectra of these substrates are presented in Figure 5f, and the extinction spectra are shown in Figure S10 (Supporting Information).

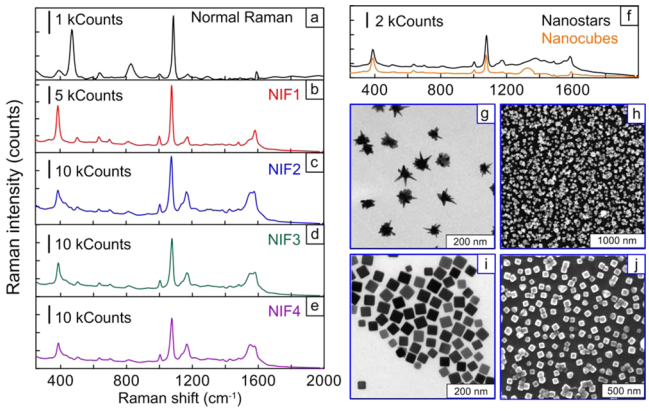

Figure 5. Normal Raman spectrum of ATP on a silicon wafer (a), SERS spectra of ATP measured with NIF1−NIF4 (b−e), self-assembled nanostars and nanocubes (f), TEM images of gold nanostars (g) and silver nanocubes (i), and SEM images of self-assembled gold nanostars (h) and silver nanocubes (j). These spectra were measured with a portable Peak Seeker Pro 785 Raman spectrometer.

The fundamental EF is the ratio of the SERS intensity I_{SERS} to the normal Raman intensity I_{Raman} normalized to the number of excited molecules[5]

DOI: 10.1021/acsami.5b01652
ACS Appl. Mater. Interfaces 2015, 7, 6518−6529

$$EF = \frac{I_{SERS}/N_{SERS}}{I_{Raman}/N_{Raman}} \quad (2)$$

where both SERS and Raman measurements should be performed under identical experimental conditions, including laser wavelength, laser power P, accumulation time t, microscope objective, spectrometer, etc. The above definition of EF presents several problems,[5] as it is difficult to estimate N_{SERS} for different substrates and to measure the Raman intensity with the same laser power and accumulation time as used for SERS measurements.

Here, we adopted a hybrid approach based on the measurement of normalized I_{SERS} and I_{Raman} intensities and on the approximate estimation of the surface density of excited molecules n_{SERS} and n_{Raman}, where P and t are the laser power and the accumulation time for both SERS and normal Raman measurements, respectively.

$$EF = \frac{[I_{SERS}/P_{SERS}t_{SERS}]/n_{SERS}}{[I_{Raman}/P_{Raman}t_{Raman}]/n_{Raman}} \quad (3)$$

This approach also is not free from obvious drawbacks. Typically, the measured SERS signal is a linear function of accumulation times, but not of the laser power P. Therefore, our calculations should be considered only as comparative estimates for similar substrates. Most difficult problem is estimation of n_{SERS} and n_{Raman}. To estimate the concentration of the adsorbed ATP per gold NIFs, their van der Waals dimensions were assumed to be 0.4 nm × 0.7 nm,[51,52] and it was assumed that the NPs or nanoislands are equally deposited on both flat sides of glass or silicon substrates. These assumptions are hardly fulfilled for real NIFs as they are not ideally flat and there are some defects on their surface. For nonfat surfaces, the number of adsorbed molecules should be increased, but owing to nonideal packing, surface defects, and steric constrains the surface per one adsorbed ATP molecule should be increased. Thus, as a first approximation, we assumed the specific surface of ATP molecules to be 1 nm^2. For comparative purposes, this assumption is quite acceptable, but the actual calculated fundamental EFs may be at least three times lower. This assumption gives the surface density of ATP molecules $n_{SERS} \approx 10^{14}$ cm^{-2} (for both substrate sides). For normal Raman measurements, 150 μL of 100 mM ATP solution was spread over a 1 cm^2 silicon slide to form a cap on the slide. During the drying process, the ATP cap was gently shacken to form a uniform yellow-colored coverage. The surface density of Raman ATP molecules $n_{Raman} \approx 9 \times 10^{18}$ cm^{-2} was estimated as follows: 150 μL × 100 mM/L × 6 × $10^{23}M^{-1}$/1 $cm^2 \approx 9 \times 10^{18}$ cm^{-2}.

Finally, any comparison of results on a flat gold surface and fabricated NIFs can be strongly affected by the difference in substrate roughness. Figure S13 (Supporting Information) gives an AFM image of NIF2 sample. The average roughness of the substrate is 4.8 nm. This value is not so high and we hope that adsorption efficiencies of our NIFs are not too different for a reasonable comparison of their SERS efficiency.

Figure 5a shows a normal Raman spectrum of ATP on a silicon wafer. In close agreement with the reported data,[53] the Raman spectrum was dominated by the ring stretching (1589 cm^{-1}), CH bending (1078 and 1034 cm^{-1}), out-of-plane bending model[54] (968 and 822 cm^{-1}), ring deformation (664 cm^{-1}), and CS stretching (389 cm^{-1}) modes. The SERS spectra fitted perfectly band to band, with similar relative intensities between the different vibrational modes for all substrates. We observed a predictable shift of lines in the SERS spectra as compared with the normal Raman spectrum. For example, CH bending appeared at 1083 cm^{-1} in the normal Raman curve and at 1078 cm^{-1} in the SERS spectra. This shift was caused by chemical adsorption of ATP molecules on the gold surface. As the 1078 cm^{-1} nCS(a1) Raman band had the highest intensity in all spectra within the total 600−2000 cm^{-1} range,[55] we compared the intensities of this band to calculate the maximal fundamental EFs of the four NIFs. All parameters used for calculations are summarized in Table 1.

Table 1. EFs Calculated for NIF1−NIF4 and for Self-Assembled Gold Nanostars and Silver Nanocubes

samples	$I_{1078} \times 10^{-2}$ (counts)	$n_{Raman,SERS}$ (cm^{-2})	$P \times t$ (mW × s)	EF
normal Raman	26.1	9×10^{18}	3×10^3	1.0
NIF1	143	10^{14}	10	1.5×10^8
NIF2	312	10^{14}	10	3.2×10^8
NIF3	270	10^{14}	10	2.7×10^8
NIF4	229	10^{14}	10	2.3×10^8
nanostars	44.0	10^{14}	10	4.5×10^7
nanocubes	19.5	10^{14}	10	2.0×10^7

The measurements led to several important conclusions. First, all experimental EFs of the four NIFs are within the close range from 1.5×10^8 to 3.2×10^8, with the best performance demonstrated by the NIF2 substrate. As it was previously suggested, the best SERS efficiency of NIF2 samples can be related with an optimal spatial distribution of grown islands and separations, which ensures the maximal surface density of electromagnetic hot spots. The experimental EF values are comparable to the best EF values obtained with quite different experimental SERS substrates, for example, immobilized nanorod assemblies (INRA)[7] and silver-coated silicon nanowires.[56] Second, the small variations in the measured EFs for all NIFs are in agreement with the FDTD calculations, which also revealed no essential differences between the surface-averaged electromagnetic EFs. Finally, the experimental EFs for all NIFs are roughly one order higher than those for assembled gold nanostars and silver nanocubes under equivalent experimental conditions. This difference between SERS performance of NIFs and assembled gold nanostars and silver nanocubes can be caused by two reasons. First, the bigger size of NIFs ensure higher enhancement of local fields. The second reason can be related to the larger gaps between nanocubes or nanostars as compared to thin gaps between nanoislands.

Clearly, Table 1 can be used for comparative purposes only as several poorly justified assumptions have been made for intermediate calculations. For detailed discussion all problems related to correct estimation of fundamental EFs, the readers are referred to excellent study by Le Ru et al.[5] As a rule, the fundamental EFs are rarely used in common laboratory practice. From a practical point of view, definition (2) is often replaced by a similar equation for the *analytical* enhancement factor (AEF).[5−7] AEF is a figure of merit that allows quantify the overall gain of signal provided by a given SERS substrate. Accordingly, AEF evaluations should be based on convenient practical measurements rather than on additional intermediated assumptions and calculations. From practical point of view, AEF compares the normal Raman signal and SERS signal for an initial and diluted analytes. The resultant

DOI: 10.1021/acsami.5b01652
ACS Appl. Mater. Interfaces 2015, 7, 6518−6529

AEF values provide a description of how much the analytical detection limit can be decreased with using a SERS substrate developed. In other words, the AEF can be defined as the ratio between SERS and Raman intensities normalized to the corresponding analyte concentrations or as the ratio between analyte concentrations that provides identical Raman and SERS intensities (note that the equations for AEFs in refs 7 and 17 should be inverted):

$$\mathrm{AEF} = \frac{[I_{\mathrm{SERS}}/c_{\mathrm{SERS}}]}{[I_{\mathrm{Raman}}/c_{\mathrm{Raman}}]} \quad (4)$$

For SERS measurements, our protocol was similar to that for determination of the detection limit. Namely, a 1 μL of 10^{-8} M ATP solution in ethanol was applied to NIFs. Immediately after drying, SERS spectra for several (typically 10) different points were measured and averaged after correction to the background signal.

For normal Raman measurements, 1 μL of 100 mM ATP solution in ethanol was applied to a silicon wafer and after drying the solution formed very thin yellow film. Figure 6

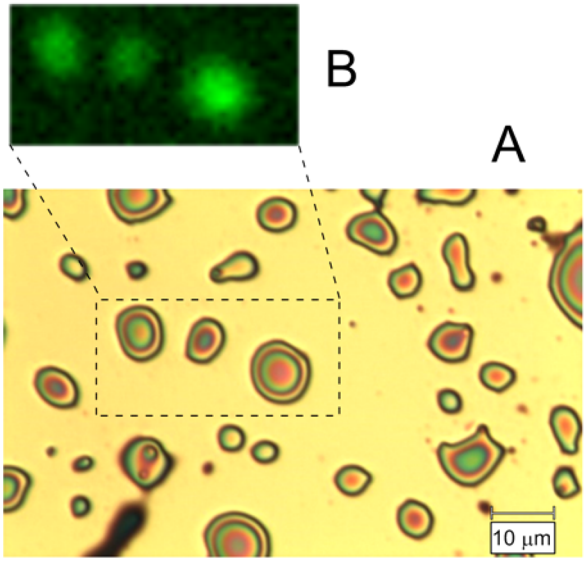

Figure 6. Distribution of dried spots of ATP on a fragment of silicon waver after application of 1 μL of 100 mM solution. Typically, the total area (A) of dried ATP spot was about of 15 mm^2 (Leica 2500 DM, bright-field image). The dashed square shows a selected area B (about of 20 × 40 μm) with three exciting ATP spots from Raman map, line 1078 cm^{-1}. The bar is 10 μm.

clearly indicated formation of small ATP spots after drying. The average size of spots varied from 1 to 10 μm. Thus, the concentration of excited ATP molecules will strongly depend on the measuring conditions, including the laser spot diameter. In our case, three spots of Raman map (Figure 6B) were randomly selected and then the average Raman intensity from all points on the selected area, including the empty ones, was measured.

By applying this approach, we were able to detect the normal Raman signal from a 100 mM ATP concentration after its drying (Supporting Information Figure S12). Of course, the instrumental detection limit can be decreased by focusing the laser spot on ATP-occupied area or to collect signal from an ensemble of ATP spots. However, the actual number of exciting ATP reporters will be questionable in this case.

For calculations of AEFs, we measured most intense SERS peak at 1078 cm^{-1} for 10^{-8} M ATP concentration and normal Raman peaks for 100 mM ATP concentration. All input data and calculated AEFs are listed in Table 2.

Table 2. Analytical Enhancement Factors (AEFs) Calculated for NIF2 and NIF3 Samples by Using Most Intense Raman Peak at 1078 cm^{-1}[a]

samples	$I_{\mathrm{Raman,SERS}} \times 10^{-3}$ (counts)	$c_{\mathrm{Raman,SERS}}$ (M)	AEF
Normal Raman	7.6	10^{-1}	1.0
NIF2	9.4	10^{-8}	1.2×10^7
NIF3	6.1	10^{-8}	0.8×10^7

[a]All experimental conditions are equal for SERS and normal Raman spectra measured with a Renishaw inVia confocal Raman microscope.

As expected, the calculated AEFs are one order lower than those for the fundamental EFs. Typically, the directly measured AEFs are less than fundamental EFs that can vary in broad limits.[5] These differences are certainly related to inaccurate estimation of actual densities of exciting ATP in Raman and, especially, SERS measurements and with significantly different laser powers used for SERS and normal Raman measurements in the case of fundamental EFs. Nevertheless, the AEF values in Table 2 are in close agreement with those reported by Zhou et al.[40]

Point-to-Point Repeatability and Sample-to-Sample Reproducibility of SERS Substrates. For successful quantitative analytical applications, the stability of SERS response is of great importance. One has to differentiate between the point-to-point repeatability of SERS spectra measured for different points of the same substrate,[57] and the sample-to-sample reproducibility[58] of SERS enhancing properties. As systematic errors of Raman measurements typically do not exceed 1%, the main contribution to variations in SERS response comes from variations in the SERS enhancement over the substrate area (point-to-point variations). Additionally, the surface density and spatial distribution of electromagnetic "hot spots" can vary from sample to sample thus giving an additional contribution to overall variations of measured SERS spectra.

To illustrate the reproducibility of our fabrication protocol, we collected SERS spectra for four NIF3 substrates obtained in four independent runs. These spectra are shown in Figure 7a without any adjustment or normalization; that is, all curves are shown as measured. Typically, we observed only 5% variations in the intensity of the main peak, whereas the maximal variations in some spectral bands were about 20%. These results are in agreement with percentage difference of 8.3% between the main averaged peaks for two independent samples obtained by Santos et al.[57] by averaging of 30 SERS spectra. However, to compare Raman signal point-to-point repeatability for the same sample, the percentage relative standard deviation (RSD%) is more representative and useful.[57,58] For example, Zhou et al.[40] reported RSD values less than 16.5% for Raman peaks at 1077, 1142, 1434, and 1578 cm^{-1}. These numbers were calculated from spatial distribution of SERS intensities measured with 45 different spots.

To obtain some rough estimation of point-to-point repeatability of our NIFs substrates, SERS spectra were first accumulated from ten randomly chosen points of a substrate. Representative examples are shown in Figure S11 (Supporting Information) for NIF1 and NIF2 and in Figure 7b and c for NIF3 and NIF4. Typically, the maximal RSD values for the

DOI: 10.1021/acsami.5b01652
ACS Appl. Mater. Interfaces 2015, 7, 6518−6529

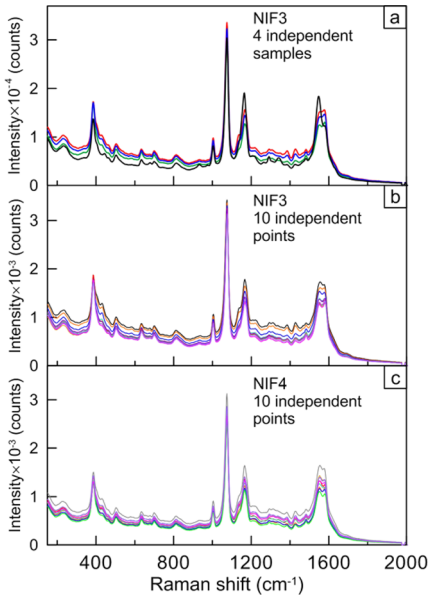

Figure 7. SERS spectra of ATP collected by using four independent NIF3 substrates (a) and SERS spectra collected at 10 points of NIF3 and NIF4 samples (b, c). The standard deviations of peak intensity at 1078 cm^{-1} are 3.4 and 5.7% for NIF3 and NIF4, respectively. These plots were measured with a portable Peak Seeker Pro 785 Raman spectrometer.

major peak at 1078 cm^{-1} did not exceed 6% in all cases. However, for Raman vibrations near 1580 cm^{-1}, RSD values were higher, about of 20%. In the current literature,[57,58] the RSD values less than 20% are typical for high quality SERS substrates with good spatial uniformity and reproducibility.

Although these estimations give some primary impression about uniformity of NIF substrates, ten spectra are not enough for reliable characterization of point-to-point repeatability. For example, Zhou et al.[40] and Que et al.[58] used 45 and 68 spots for characterization of spatial SERS peak distributions and RSD calculations. To further assess the reproducibility of SERS signals, the RSDs of major peaks was estimated from Raman maps. To this end, several new NIF2 and NIF3 samples were fabricated through independent runs and then Raman maps were collected for 800 points with 1 μm increment in $X-Y$ directions. Figure 8 shows a representative example for NIF2 and NIF3 samples, where Raman maps with different colors indicate the spatial distribution of Raman peaks of 10^{-8} M ATP at 968, 1078, and 1589 cm^{-1}. Qualitatively, the more uniform is the color distribution, the better is point-to-point repeatability.

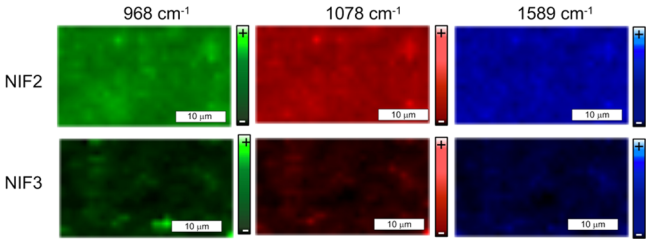

Figure 8. Raman maps for NIF2 and NIF3 samples, fabricated through independent runs. Green, red, and blue colors correspond to ATP peaks at 968, 1078, and 1589 cm^{-1}. The columns on right represent variations in peak intensities. For measurements, 1 μL of 10^{-8} ATP was applied to substrates. The bars are 10 μm.

In Figure 8, NIF2 sample clearly demonstrates better point-to-point repeatability as compared to NIF3 substrate. For quantitative estimations of RSD%, the intensity variations for three selected peaks at 968, 1078, and 1589 cm^{-1} are shown in Figure 9 for 50 randomly chosen spots in Raman maps (1 μL of

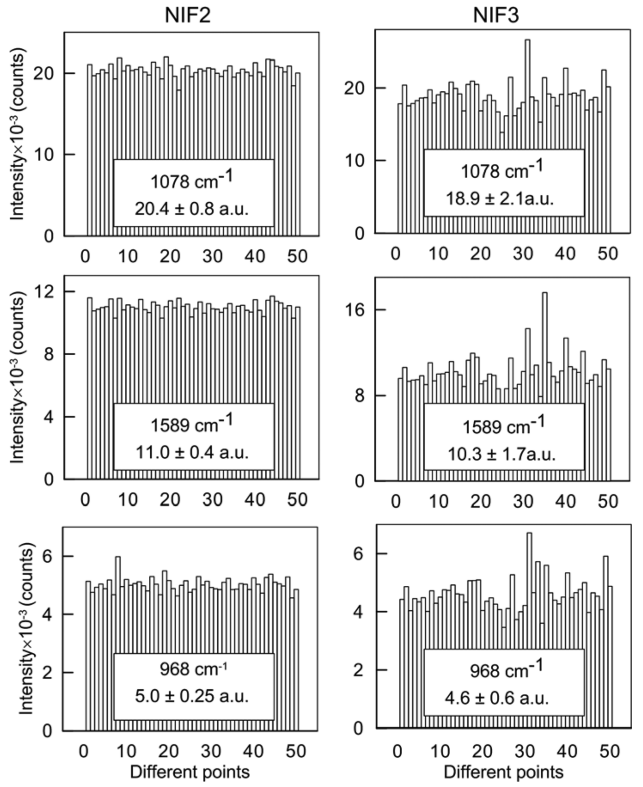

Figure 9. Intensities of the Raman peaks of ATP at 968, 1078, and 1589 cm^{-1} in 50 different points. For measurements, 1 μL of 10^{-8} ATP was applied to substrates.

10^{-8} ATP). It follows from data of Figure 9, that RSD percentages for NIF2 sample are 3.9% (1078 cm^{-1}), 3.6% (1589 cm^{-1}), and 5% (968 cm^{-1}). It should be emphasized, that these RSD percentages are in good agreement with RSDs obtained for major 1078 cm^{-1} peak with independent fabrication runs and only with 10 measured spectra (Supporting Information Figure S11, Peak Seeker Pro 785 device). However, the RSD percentages of NIF3 samples, derived from Raman maps, are somewhat higher than those shown in Figure 7. Specifically, for NIF3 sample in Figure 9, we obtained the following RSD%: 11.1% (1078 cm^{-1}), 16.5% (1589 cm^{-1}), and 13.0% (968 cm^{-1}).

In general, both the simplified test with ten measurements by Peak Seeker Pro 785 Raman spectrometer and more sophisticated Raman map tests with Renishaw inVia confocal Raman microscope revealed excellent point-to-point repeatability and sample-to-sample reproducibility of SERS measurements with the fabricated NIFs. Thus, the fabricated NIFs can be used in those applications in which reproducibility over a large area or across multiple measurements is a crucial point.

SERS Detection of Thiram. Thiram is an ectoparasiticide that is often used to prevent fungal diseases in seed and crops and as an animal repellent to protect fruit trees and ornamentals from damage by rabbits, rodents, and deer. Thiram is moderately toxic by ingestion but is highly toxic if inhaled. Acute exposure in humans may cause headaches,

DOI: 10.1021/acsami.5b01652
ACS Appl. Mater. Interfaces 2015, 7, 6518−6529

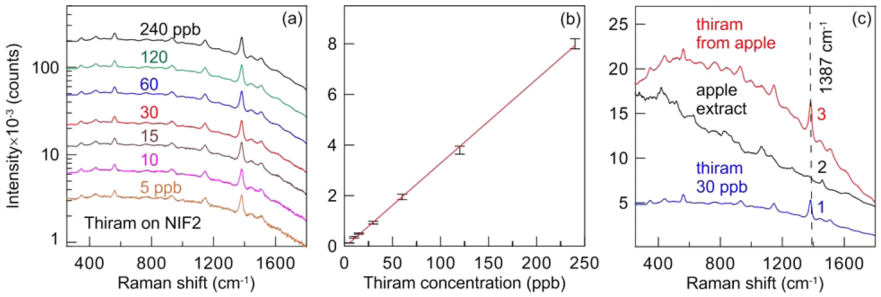

Figure 10. (a) SERS spectra of thiram obtained from 1 μL of a thiram methanol solution [concentration, 5−240 ppb (20 fM−1 nM)] by using the NIF2 substrate. (b) Calibration curve for the determination of the thiram concentration from the SERS intensity at 1387 cm^{-1}. The error bars represent the standard deviations, n = 4. (c) SERS spectra of thiram (1 μL, 30 ppb, curve 1), an extract from an uncontaminated apple (2), and an extract from an apple peel contaminated with thiram (3). Note the logarithmic ordinate scale in the panel (a). For details, see Methods.

dizziness, fatigue, nausea, diarrhea, and other gastrointestinal complaints.[59] For real-life SERS detection of pesticides, such important problems should be solved as extraction, purification, and sorption on a SERS platform. From this point of view, thiram appears promising for testing gold NIFs. Indeed, the fungicide is fully insoluble in water but is soluble in nonpolar solvents, thus making it easy to extract from fruits. Further, thiram has a disulfide bond which spontaneously breaks on exposure to the gold surface and binds to gold NIFs through the Au−S bond. SERS spectra for thiram have been reported and the modes of its binding to silver colloids and gold films have been discussed.[60,61] Additionally, low-level detection of thiram by using silver nanoshells[62] and gold nanorods[63] as SERS platforms has been addressed. In this article, we measured the SERS spectra of a thiram methanol solution and of a methanol extract of thiram from apple peels.

Figure 10 shows a representative set of SERS spectra (a) and a calibration curve (b) of the SERS intensity at 1387 cm^{-1} as a function of the thiram concentration. These plots were obtained with the NIF2 substrate. For convenient representation, the intensity (y-axis) is given on a log scale. Several peaks are clearly seen within the 200−2000 cm^{-1} shift range. In good agreement with previously reported data,[63,64] the major peak at 1387 cm^{-1} can be attributed to the CN stretching mode and to the symmetric CH_3 deformation mode. Since this is the strongest peak in the SERS spectra, this band was used to calibrate the SERS intensity as a function of the thiram concentration.

In general, the basic characteristic peaks were in line with previous observations:[63] the asymmetric CH_3 deformation mode (1444 cm^{-1}), the CN stretching and CH_3 rocking modes (1508 cm^{-1}), the stretching CH_3N and C═S modes (928 cm^{-1}), and the SS stretching mode (556 cm^{-1}). The intensity of the major peak at 1387 cm^{-1} depended linearly on the thiram concentration up to 250 ppb. It should be noted that the detection limit in our case (about 20 fM) was at least 1000 times lower than the previously reported value (43 nM[63]). Such significant improvement in detection sensitivity might be attributed to the higher EF of our NIF2 substrate, as compared with that of assembled dog-bone shaped nanorods.[63]

The large enhancement of the Raman signal from thiram molecules with the NIF2 platform suggests good promise for potential real-life detection of thiram on fruit peels. For validating this suggestion, apple peels were cut into squares of 1 cm^2, and 1 μL of 5 ppm thiram solutions was dropped onto the peel surface. After the solvent had evaporated, the peel was placed in 0.5 mL of methanol for 3 min. The negative control was uncontaminated peels, and the positive control was a 30 ppb methanol solution of thiram. One μL of each sample was spotted on a 1 × 1 cm NIF2 substrate, so that at least 10 simultaneous probes could be tested with a single NIF.

Figure 10c shows the SERS spectra of thiram traces collected from a thiram-contaminated apple peel. The characteristic bands of thiram are clearly seen against the background of the uncontaminated apple extract. The intensity of the strongest peak is comparable to that obtained from a 30 ppb methanol solution of the fungicide. Thus, the NIF2 SERS platform can be used for fast real-life detection of thiram at 4.8 ng/cm^2, which is almost one order lower than previously reported detection limit (38 ng/cm^2)[41] and much lower than the permissible level for apple peels (2 μg/cm^2).[62]

CONCLUSION

In conclusion, we have employed a simple wet-chemical approach to fabricating centimeter-scale gold NIF substrates with high SERS sensitivity and with excellent reproducibility. The optimized NIFs have demonstrated the Raman scattering EF of 3 × 10^8, as found by use of ATP reporters. In principle, such EFs are large enough to enable detection of single-molecule responses.[5] Variations in SERS response were as low as 6% in point-to-point and batch-to-batch measurements. As the large-area NIFs are easy and cheap to make, they can be helpful in label-free immunoassays, biosensing, and fast detection of pesticides. As an example, thiram fungicide concentrations at least 100-fold lower than the level currently permissible in farming have been fast detected on apple peels. Specifically, the NIF-based label-free SERS technology detected thiram on apple peel down to level of 5 ng/cm^2.

METHODS

Materials. The following reagents were used: 1,4-aminothiophenol (ATP, 99%; Sigma−Aldrich), $AgNO_3$ (>99.9%; Aldrich; 20.913−9), ethylene glycol (EG) (99%, Aldrich; 293237), poly(vinylpyrrolidone) (PVP) (M_w = 55000; Sigma-Aldrich; 85.656−8), isopropyl alcohol (IPA) (chemical grade; Vekton Co., Russia), 30% aqueous solution of ammonia (Aldrich), acetone (chemical grade; Vekton, Russia), absolute ethanol (99.99%; Sharlau; 64-17-5), $Na_2S{\cdot}9H_2O$ (analytical grade; Radian Co., Russia), ascorbic acid (>99%, Aldrich), (3-mercaptopropyl)trimethoxysilane (MPTMS, 98%; Aldrich), condensed argon (99.99%), tetrachloroauric acid (>99%; Sigma-Aldrich), nitric acid (chemical grade; GOST 4461-77; Radian, Russia), hydrochloric acid (chemical grade; GOST 3118-77; Radian, Russia), Milli-Q water (18 MOhm × cm; Millipore), and a commercially available thiram solution (250 mg/mL; Avgust Co., Russia). Standard microscopic cover glass and silicon wafers were used as hard templates for NIF fabrication.

DOI: 10.1021/acsami.5b01652
ACS Appl. Mater. Interfaces 2015, 7, 6518−6529

Fabrication of Gold NIFs. First, 13 nm spherical Au nanoparticles were prepared as described by Grabar et al.[65] Concentration of NPs 6 × 10^{12} particles/mL was estimated from optical density measurements.[66] Microscopic cover glasses and silicon wafers were cut into 1 × 1 cm slides. The slides were cleaned by immersion in an as-prepared piranha solution (H_2SO_4/H_2O_2, 1:3) for 30 min and were washed several times in water and ethanol. Next, each slide was incubated in 10% MPTMS in an ethanol solution for 1 h, and the slides were rinsed several times with ethanol and water. For chemisorption of gold nanoparticles on the thiol-functionalized surface, each slide was incubated in 3 mL of a colloidal gold solution for 3 h and then rinsed with water. NIFs were fabricated by additional reduction of gold on the surface of the slides with gold nanoparticles attached. Each slide was placed in 3 mL of water, after which 18 μL of 4% $HAuCl_4$, 10 μL of 1 M HCl, 45 μL of 2 mM $AgNO_3$, and 90 μL of 100 mM of AA were subsequently added under vigorous mixing. For preparation of NIF films with different gold coating densities, the overgrowth procedure was applied several times (1 to 4) under the same conditions and reagent concentrations. All samples were dried with air flow and stored in ethanol until used.

Fabrication of Nanocubes, Nanostars, and Self-Assembled Films. Ag nanocubes were fabricated as described elsewhere.[67,68] Briefly, 30 mL of EG was added to a 250 mL round-bottomed flask and was heated in an oil bath at 150 °C under magnetic stirring. After 50 min preheating, argon was introduced at a flow rate of 1200 mL/min. Ten min after, a sodium sulfide solution in EG (0.35 mL, 3 mM) was quickly injected into the preheated EG solution, followed by injection of a PVP solution in EG (7.5 mL, 20 g/L) and 8 min later by injection of a silver nitrate solution in EG (2.5 mL, 48 g/L). The reaction time was 30 min. The Ag nanocubes were collected by centrifugation and redispersion in 40 mL of ethanol. For synthesis of nanostars, we used a slightly modified[17] protocol of Yan et al.[69] Specifically, 3 mL of solutions of 13 nm citrate-stabilized seeds was added to 100 mL of 0.75 mM $HAuCl_4$ with 300 μL of 1 M HCl in a 200 mL glass vial at room temperature under moderate stirring (700 rpm). At the same time, 3 mL of 2 mM silver nitrate and 1.5 mL of 100 mM AA were quickly added. The solution was stirred for 30 s, as its color rapidly turned from light red to blue or green. The self-assembled arrays of nanocubes and nanostars were obtained by using the same protocol as applied for chemisorptions of 13 nm seeds.

Measurements. TEM images were obtained with a Libra-120 transmission electron microscope (Carl Zeiss, Germany). A 10 μL drop of nanoparticles suspension was placed on a 300 mesh Formvar-coated copper microscopic grid. TEM images were recorded under 120 kV (magnification, ×10000−40000). For TEM imaging of NIFs, a glass slide with a gold film was gently placed in a concentrated HF solution to make the gold film float on the HF surface. This layer was gently picked up with the grid, washed with water, dried, and examined by TEM. SEM images of gold NIFs and nanoparticles on silicon wafers were obtained with a MiraTescan scanning electron microscope under 30 kV. Extinction spectra were recorded with a Specord BS-250 UV−vis spectrophotometer (Analytik Jena, Germany).

SERS and Raman Measurements of ATP. For SERS measurements with Peak Seeker Pro 785 Raman spectrometer (Figure 5 and Supporting Information Figure S11), NIFs and self-assembled nanoparticle arrays were incubated in 100 μM ATP solution in ethanol for 1 h. The slides were rinsed with ethanol and water, dried with argon flow, and stored under argon until use. For normal Raman measurements, 150 μL of 100 mM ATP solution was spread over a 1 cm^2 silicon slide to form a cap on the slide. During the drying process, the ATP cap was gently shacken to form a uniform yellow-colored coverage. In both procedures, thiol group of 1,4-aminothiophenol ATP links to gold. SERS and Raman spectra were recorded with a Peak Seeker Pro 785 Raman spectrometer (Ocean Optics) under 785 nm irradiation (10 mW for SERS and 300 mW for Raman measurements, respectively). The SERS and Raman acquisition intervals were 1 and 100 s, respectively. All SERS spectra were averaged over 10 independent runs with equivalent focusing conditions. SERS detection of thiram was also performed with portable Peak Seeker Pro 785 device.

For determination of SERS sensitivity, detection limits, Raman maps (20 × 40 spectral points over each sample, 1 μm increment in *X*−*Y* directions), and point-to-point repeatability of selected Raman peaks, a Renishaw inVia confocal Raman microscope was used. The optical part of the device is equipped with a Leica DM 2500 optical microscope. The corresponding experimental protocols are described in the main text.

SERS Measurements of Thiram in Methanol Solutions and Thiram on Apple Peels. The thiram fungicide was diluted with methanol to weight concentrations ranging from 240 to 5 ppb. A 1 μL of thiram solution was spotted on a NIF2 substrate, and SERS spectra were collected under standard conditions (785 nm, 10 mW, 10 s).

Green apples purchased from a local grocery store were used. A 1 μL drop of a 5 ppm solution of thiram in methanol was applied to the apple to artificially contaminate it with the fungicide. After the solution had dried, about 1 cm^2 of the peel was removed and placed in 500 μL of methanol. Then, 10 μL of the extract was spotted on a NIF2 substrate, and SERS spectra were collected under standard conditions (785 nm, 10 mW, 10 s). The negative control was uncontaminated apple peels, and the positive control was a 30 ppb methanol solution of thiram.

FDTD Simulations. FDTD simulations of field distributions were made with the commercially available software Lumerical FDTD Solutions 8. To design an NI model for simulations, a magnified 300 × 300 nm TEM image of an NIF with different overgrowth rates (NIF1−NIF4) was uploaded to make a 2D *XY* projection. The thickness of all films in the *Z*-direction was chosen to be 30 nm. The simulation volume was a 300 × 300 × 100 nm parallelepiped with a uniform mesh of 0.5 nm. In all simulations, the total "field/scattering field" mode under 785 nm excitation was used together with the gold optical constants taken from the Drude approximation of the Johnson and Christy data.[70] The FDTD "Field monitors" were placed in the middle and top sections of the NIF. The CPU time of one simulation run was about 48 h (4 × 2.2 GHz processors, 20 Gb RAM).

■ ASSOCIATED CONTENT

Supporting Information

SEM images of 13 nm gold nanoparticles chemisorbed on a silicon wafer, extinction spectra of a solution of 13 nm colloidal gold before and after incubation of a thiolated wafer, calculations of the surface density of the seeds, extinction spectra of glass coverslips with 13 nm chemisorbed gold seeds, SEM images of gold microstars obtained during overgrowth under different conditions, SEM images of NIF1−NIF4 at different magnifications, binarized TEM images of NIF1−NIF4 and calculation of the density of surface coverage by ATP, SEM of NIF4, FDTD simulations of field distribution at a 0.5 nm distance from the NIF1−NIF4 surfaces, SEM image of a layer of nanostars, extinction spectra of nanocubes and nanostars self-assembled on glass, SERS spectra collected at ten independent points of the NIF1 and NIF2 samples, normal Raman spectrum of 100 mM ATP on a silicon wafer, and AFM image of a NIF2 substrate. This material is available free of charge via the Internet at http://pubs.acs.org.

■ AUTHOR INFORMATION

Corresponding Author

*E-mail: khlebtsov@ibppm.sgu.ru.

Notes

The authors declare no competing financial interest.

■ ACKNOWLEDGMENTS

This research was supported by the Russian Scientific Foundation (project no. 14-13-01167). Raman map measurements by D.N.B. were supported by grant no. 14.Z50.31.0004 from the Government of the Russian Federation. E.V.P. and

DOI: 10.1021/acsami.5b01652
ACS Appl. Mater. Interfaces 2015, 7, 6518−6529

V.A.K. were partly supported by scholarships from the President of the Russian Federation.

REFERENCES

(1) Pieczonka, N. P. W.; Aroca, R. F. Single Molecule Analysis by Surfaced-Enhanced Raman Scattering. *Chem. Soc. Rev.* **2008**, *37*, 946−954.
(2) Haynes, C. L.; Yonzon, C. R.; Zhang, X.; Van Duyne, R. Surface-Enhanced Raman Sensors: Early History and the Development of Sensors for Quantitative Biowarfare Agent and Glucose Detection. *J. Raman Spectrosc.* **2005**, *36*, 471−484.
(3) Pelton, M.; Aizpurua, J.; Bryant, G. Metal-Nanoparticle Plasmonics. *Laser Photonics Rev.* **2008**, *2*, 136−159.
(4) Moskovits, M. Surface-Enhanced Spectroscopy. *Rev. Mod. Phys.* **1985**, *57*, 783−826.
(5) Le Ru, E. C.; Blackie, E.; Meyer, M.; Etchegoin, P. G. Surface Enhanced Raman Scattering Enhancement Factors: a Comprehensive Study. *J. Phys. Chem. C* **2007**, *111*, 13794−13803.
(6) Greeneltch, N. G.; Blaber, M. G.; Schatz, G. C.; Van Duyne, R. P. Plasmon-Sampled Surface-Enhanced Raman Excitation Spectroscopy on Silver Immobilized Nanorod Assemblies and Optimization for Near Infrared (λ_{ex} = 1064 nm) Studies. *J. Phys. Chem. C* **2013**, *117*, 2554−2558.
(7) Greeneltch, N. G.; Blaber, M. G.; Henry, A.-I.; Schatz, G. C.; Van Duyne, R. P. Immobilized Nanorod Assemblies: Fabrication and Understanding of Large Area Surface-Enhanced Raman Spectroscopy Substrates. *Anal. Chem.* **2013**, *85*, 2297−2303.
(8) Fan, M. K.; Andrade, G. F. S.; Brolo, A. G. A Review on the Fabrication of Substrates for Surface Enhanced Raman Spectroscopy and their Applications in Analytical Chemistry. *Anal. Chim. Acta* **2011**, *693*, 7−25.
(9) Xue, M.; Zhang, Z.; Zhu, N.; Wang, F.; Zhao, X. S.; Cao, T. Transfer Printing of Metal Nanoparticles with Controllable Dimensions, Placement, and Reproducible Surface-Enhanced Raman Scattering Effects. *Langmuir* **2009**, *25*, 4347−4351.
(10) Baia, M.; Baia, L.; Astilean, S. Gold Nanostructured Films Deposited on Polystyrene Colloidal Crystal Templates for Surface-Enhanced Raman Spectroscopy. *Chem. Phys. Lett.* **2005**, *404*, 3−8.
(11) Wei, A. Calixarene-Encapsulated Nanoparticles: Self-Assembly into Functional Nanomaterials. *Chem. Commun.* **2006**, 1581−1591.
(12) Hu, X.; Cheng, W.; Wang, T.; Wang, Y.; Wang, E.; Dong, S. Fabrication, Characterization, and Application in SERS of Self-Assembled Polyelectrolyte-Gold Nanorod Multilayered Films. *J. Phys. Chem. B* **2005**, *109*, 19385−19389.
(13) Doherty, M. D.; Murphy, A.; McPhillips, J.; Pollard, R. J.; Dawson, P. Wavelength Dependence of Raman Enhancement from Gold Nanorod Arrays: Quantitative Experiment and Modeling of a Hot Spot Dominated System. *J. Phys. Chem. C* **2010**, *114*, 19913−19919.
(14) Álvarez-Puebla, R. A.; Agarwal, A.; Manna, P.; Khanal, B. P.; Aldeanueva-Potel, P.; Carbó-Argibay, E.; Pazos-Pérez, N.; Vigderman, L.; Zubarev, E. R.; Kotov, N. A.; Liz-Marzán, L. M. Gold Nanorods 3D-Supercrystals as Surface-Enhanced Raman Scattering Spectroscopy Substrates for the Rapid Detection of Scrambled Prions. *Proc. Natl. Acad. Sci. U. S. A.* **2011**, *108*, 8157−8161.
(15) Khlebtsov, B. N.; Khanadeev, V. A.; Tsvetkov, M. Yu.; Bagratashvili, V. N.; Khlebtsov, N. G. Surface-Enhanced Raman Scattering Substrates Based on Self-Assembled PEGylated Gold and Gold−Silver Core−Shell Nanorods. *J. Phys. Chem. C* **2013**, *117*, 23162−23171.
(16) Esenturk, E. N.; Hight Walker, A. R. Surface-Enhanced Raman Scattering Spectroscopy via Gold Nanostars. *J. Raman Spectrosc.* **2009**, *40*, 86−91.
(17) Khlebtsov, B. N.; Panfilova, E. V.; Khanadeev, V. A.; Khlebtsov, N. G. Improved Size-Tunable Synthesis and SERS Properties of Au Nanostars. *J. Nanopart. Res.* **2014**, *16*, 2623.
(18) Rodríguez-Lorenzo, L.; de la Rica, R.; Álvarez-Puebla, R. A.; Liz-Marzán, L. M.; Stevens, M. M. Plasmonic Nanosensors with Inverse Sensitivity by Means of Enzyme-Guided Crystal Growth. *Nat. Mater. (Lett.)* **2012**, *11*, 604−607.
(19) Sajanlal, P. R.; Pradeep, T. Mesoflowers: A New Class of Highly Efficient Surface-Enhanced Raman Active and Infrared-Absorbing Materials. *Nano Res.* **2009**, *2*, 306−320.
(20) Hamon, C.; Postic, M.; Mazari, E.; Bizien, T.; Dupuis, C.; Even-Hernandez, P.; Jimenez, A.; Courbin, L.; Gosse, C.; Artzner, F.; et al. Three-Dimensional Self-Assembling of Gold Nanorods with Controlled Macroscopic Shape and Local Smectic B Order. *ACS Nano* **2012**, *6*, 4137−4146.
(21) Hamon, C.; Novikov, S.; Scarabelli, L.; Basabe-Desmonts, L.; Liz-Marzán, L. M. Hierarchical Self-Assembly of Gold Nanoparticles into Patterned Plasmonic Nanostructures. *ACS Nano* **2014**, *8*, 10694−10700.
(22) Zhou, Y.; Zhou, X.; Park, D. J.; Torabi, K.; Brown, K. A.; Jones, M. R.; Zhang, C.; Schatz, G. C.; Mirkin, C. A. Shape-Selective Deposition and Assembly of Anisotropic Nanoparticles. *Nano Lett.* **2014**, *14*, 2157−2161.
(23) Tsvetkov, M. Yu.; Khlebtsov, B. N.; Khanadeev, V. A.; Bagratashvili, V. N.; Timashev, P. S.; Samoylovich, M. I.; Khlebtsov, N. G. SERS Substrates Formed by Gold Nanorods Deposited on Colloidal Silica Films. *Nanoscale Res. Lett.* **2013**, *8*, 250.
(24) Khanadeev, V. A.; Khlebtsov, B. N.; Klimova, S. A.; Tsvetkov, M. Yu.; Bagratashvili, V. N.; Sukhorukov, G. B.; Khlebtsov, N. G. Large-Scale High-Quality 2D Silica Crystals: Dip-Drawing Formation and Decoration with Gold Nanorods and Nanospheres for SERS Analysis. *Nanotechnology* **2014**, *25*, 405602.
(25) Natan, M. J. Concluding Remarks. Surface Enhanced Raman Scattering. *Faraday Discuss.* **2006**, *132*, 321−328.
(26) Pavaskar, P.; Hsu, I.-K.; Theiss, J.; Hung, W. H.; Cronin, S. B. A Microscopic Study of Strongly Plasmonic Au and Ag Island Thin Films. *J. Appl. Phys.* **2013**, *113*, No. 034302.
(27) Aroca, R.; Martin, F. Tuning Metal Island Films for Maximum Surface-Enhanced Raman Scattering. *J. Raman Spectrosc.* **1985**, *16*, 156−162.
(28) Zhang, J.; Yu, h.-Z.; Zhao, J.; Liu, Z.-F.; Li, H.-L. SEIR and SERS of an Azobenzene Acid Monolayer on Silver Island Films. *Appl. Spectrosc.* **1999**, *53*, 1305−1308.
(29) Chang, G.; Zhang, J.; Oyama, M.; Hirao, K. Silver-Nanoparticle-Attached Indium Tin Oxide Surfaces Fabricated by a Seed-Mediated Growth Approach. *J. Phys. Chem. B* **2005**, *109*, 1204−1209.
(30) Sanchez-Iglesias, A.; Aldeanueva-Potel, P.; Ni, W.; Perez-Juste, J.; Pastoriza-Santos, I.; Alvarez-Puebla, R. A.; Mbenkum, B. N.; Liz-Marzan, L. M. Chemical Seeded Growth of Ag Nanoparticle Arrays and Their Application as Reproducible SERS Substrates. *Nano Today* **2010**, *5*, 21−27.
(31) Kambayashi, M.; Zhang, J.; Oyama, M. Crystal Growth of Gold Nanoparticles on Indium Tin Oxides in the Absence and Presence of 3-Mercaptopropyl-trimethoxysilane. *Cryst. Growth Des.* **2005**, *5*, 81−84.
(32) Umar, A. A.; Oyama, M. Growth of High-Density Gold Nanoparticles on an Indium Tin Oxide Surface Prepared Using a "Touch" Seed-Mediated Growth Technique. *Cryst. Growth Des.* **2005**, *5*, 599−607.
(33) Kumar, S.; Yang, H.; Zou, S. Seed-Mediated Growth of Uniform Gold Nanoparticle Arrays. *J. Phys. Chem. C* **2007**, *111*, 12933−12938.
(34) He, L.; Lamont, E.; Veeregowda, B.; Sreevatsan, S.; Haynes, C. L.; Diez-Gonzalez, F.; Labuza, T. P. Aptamer-Based Surface-Enhanced Raman Scattering Detection of Ricin in Liquid Foods. *Chem. Sci.* **2011**, *2*, 1579−1582.
(35) Craig, A. P.; Franca, A. S.; Irudayaraj, J. Surface-Enhanced Raman Spectroscopy Applied to Food Safety. *Annu. Rev. Food Sci. Technol.* **2013**, *4*, 369−380.
(36) Alak, A. M.; Vo-Dinh, T. Surface-Enhanced Raman Spectroscopy of Organophosphorous Chemical Agents. *Anal. Chem.* **1987**, *59*, 2149−2153.
(37) Fodjo, E. K.; Riaz, S.; Li, D.-W.; Qu, L.-L.; Marius, N. P.; Trokourey, A.; Long, Y.-T. Cu@Ag/β-$AgVO_3$ as a SERS Substrate for

DOI: 10.1021/acsami.5b01652
ACS Appl. Mater. Interfaces 2015, 7, 6518−6529

the Trace Level Detection of Carbamate Pesticides. *Anal. Methods* **2012**, *4*, 3785−3791.
(38) Liu, B.; Han, G.; Zhang, Z.; Liu, R.; Jiang, C.; Wang, S.; Han, M. Y. Shell Thickness-Dependent Raman Enhancement for Rapid Identification and Detection of Pesticide Residues at Fruit Peels. *Anal. Chem.* **2012**, *84*, 255−261.
(39) Tang, X.; Cai, W.; Yang, L.; Liu, J. Highly Uniform and Optical Visualization of SERS Substrate for Pesticide Analysis Based on Au Nanoparticles Grafted on Dendritic α-Fe_2O3. *Nanoscale* **2013**, *5*, 11193−11199.
(40) Zhou, X.; Zhou, F.; Liu, H.; Yang, L.; Liu, J. Assembly of Polymer−Gold Nanostructures with High Reproducibility into a Monolayer Film SERS Substrate with 5 nm Gaps for Pesticide Trace Detection. *Analyst* **2013**, *138*, 5832−5838.
(41) Yang, J.-K.; Kang, H.; Lee, H.; Jo, A.; Jeong, S.; Jeon, S.-J.; Kim, H.-I.; Lee, H.-Y.; Jeong, D. H.; Kim, J.-H.; Lee, Y.-S. Single-Step and Rapid Growth of Silver Nanoshells as SERS-Active Nanostructures for Label-Free Detection of Pesticides. *ACS Appl. Mater. Interfaces* **2014**, *6*, 12541−12549.
(42) Shende, S.; Inscore, F.; Sengupta, A.; Stuart, J.; Farquharson, S. Rapid Extraction and Detection of Trace Chlorpyrifos-Methyl in Orange Juice by Surface-Enhanced Raman Spectroscopy. *Sens. Instrum. Food. Qual.* **2010**, *4*, 101−107.
(43) Ye, J.; Bonroy, K.; Nelis, D.; Frederix, F.; D'Haen, J.; Maes, G.; Borghs, G. Enhanced Localized Surface Plasmon Resonance Sensing on Three-Dimensional Gold Nanoparticles Assemblies. *Colloid. Surface. A* **2008**, *321*, 313−317.
(44) Lafuma, A.; Quere, D. Superhydrophobic States. *Nat. Mater.* **2003**, *2*, 457−460.
(45) Khlebtsov, B. N.; Zharov, V. P.; Melnikov, A. G.; Tuchin, V. V.; Khlebtsov, N. G. Optical Amplification of Photothermal Therapy with Gold Nanoparticles and Nanoclusters. *Nanotechnology* **2006**, *17*, 5167−5179.
(46) Khlebtsov, B. N.; Khanadeyev, V. A.; Ye, J.; Mackowski, D. W.; Borghs, G.; Khlebtsov, N. G. Coupled Plasmon Resonances in Monolayers of Metal Nanoparticles and Nanoshells. *Phys. Rev. B* **2008**, *77*, No. 035440.
(47) Camden, J. P.; Dieringer, J. A.; Wang, Y.; Masiello, D. J.; Marks, L. D.; Schatz, G. C.; van Duyne, R. P. Probing the Structure of Single-Molecule Surface-Enhanced Raman Scattering Hot Spots. *J. Am. Chem. Soc.* **2008**, *130*, 12616−12617.
(48) Khlebtsov, B. N.; Melnikov, A. G.; Zharov, V. P.; Khlebtsov, N. G. Absorption and Scattering of Light by a Dimer of Metal Nanospheres: Comparison of Dipole and Multipole Approaches. *Nanotechnology* **2006**, *17*, 1437−1445.
(49) Quinten, M. *Optical Properties of Nanoparticle Systems*; Wliey-VCH Verlag: Weinheim, Germany, 2011.
(50) McFarland, A. D.; Young, M. A.; Dieringer, J. A.; Van Duyne, R. P. Wavelength-Scanned Surface-Enhanced Raman Excitation Spectroscopy. *J. Phys. Chem. B* **2005**, *109*, 11279−11285.
(51) Nikoobakht, B.; W, J.; El-Sayed, M. A. Surface-Enhanced Raman Scattering of Molecules Adsorbed on Gold Nanorods: Off-Surface Plasmon Resonance Condition. *Chem. Phys. Lett.* **2002**, *366*, 17−23.
(52) Chang, S.-C.; Chao, I.; Tao, Y.-T. Structures of Self-Assembled Monolayers of Aromatic-Derivatized Thiols on Evaporated Gold and Silver Surfaces: Implication on Packing Mechanism. *J. Am. Chem. Soc.* **1994**, *116*, 6792−6805.
(53) Ye, J.; Hutchison, J. A.; Uji, H.; Hofkens, J.; Lagae, L.; Maes, G.; Borghs, G.; Van Dorpe, P. Excitation Wavelength Dependent Surface Enhanced Raman Scattering of 4-Aminothiophenol on Gold Nanorings. *Nanoscale* **2012**, *4*, 1606−1611.
(54) Dendisová, M.; Havránek, L.; Ončák, M.; Matějka, P. In Situ SERS Study of Azobenzene Derivative Formation from 4-Aminobenzenethiol on Gold, Silver, and Copper Nanostructured Surfaces: What Is the Role of Applied Potential and Used Metal? *J. Phys. Chem. C* **2013**, *117*, 21245−21253.
(55) Osawa, M.; Matsuda, N.; Yoshii, K.; Uchida, I. Charge Transfer Resonance Raman Process in Surface-Enhanced Raman Scattering from *p*-Aminothiophenol Adsorbed on Silver: Herzberg−Teller Contribution. *J. Phys. Chem.* **1994**, *98*, 12702−12707.
(56) Galopin, E.; Barbillat, J.; Coffinier, Y.; Szunerits, S.; Patriarche, G.; Boukherroub, R. Silicon Nanowires Coated with Silver Nanostructures as Ultrasensitive Interfaces for Surface-Enhanced Raman Spectroscopy. *ACS Appl. Mater. Interfaces* **2009**, *1*, 1396−1403.
(57) Santos, E. B.; Sigoli, F. A.; Mazali, I. O. Surface-Enhanced Raman Scattering of 4-Aminobenzenethiol on Silver Nanoparticles Substrate. *Vib. Spectrosc.* **2013**, *68*, 246−450.
(58) Que, R.; Shao, M.; Zhuo, S.; Wen, C.; Wang, S.; Lee, S.-T. Highly Reproducible Surface-Enhanced Raman Scattering on a Capillarity-Assisted Gold Nanoparticle Assembly. *Adv. Funct. Mater.* **2011**, *21*, 3337−3343.
(59) Ray, D. E. Pesticides Derived From Plants and Other Organisms. In *Handbook of Pesticide Toxicology*; Hayes, W. J., Jr., Laws, E. R., Jr., Eds.; Academic Press: New York, 1991; pp 10−144.
(60) Sanchez-Cortes, S.; Vasina, M.; Francioso, O.; Garcia-Ramos, J. V. Raman and Surface-Enhanced Raman Spectroscopy of Dithiocarbamate fungicides. *Vib. Spectrosc.* **1998**, *17*, 133−144.
(61) Sanchez-Cortes, S.; Domingo, C. J.; Garcia-Ramos, V.; Aznarez, J. A. Surface-Enhanced Vibrational Study (SEIR and SERS) of Dithiocarbamate Pesticides on Gold Films. *Langmuir* **2001**, *17*, 1157−1162.
(62) Yang, J.-K.; Kang, H.; Lee, H.; Jo, A.; Jeong, S.; Jeon, S.-J.; Kim, H.-I.; Lee, H.-Y.; Jeong, D. H.; Kim, J.-H.; Lee, Y. S. Single-Step and Rapid Growth of Silver Nanoshells as SERS-Active Nanostructures for Label-Free Detection of Pesticides. *ACS Appl. Mater. Interfaces* **2014**, *6*, 12541−12549.
(63) Saute, B.; Narayanan, R. Solution-Based Direct Readout Surface Enhanced Raman Spectroscopic (SERS) Detection of Ultra-Low Levels of Thiram with Dogbone Shaped Gold Nanoparticles. *Analyst* **2011**, *136*, 527−532.
(64) Kang, J. S.; Hwang, S. Y.; Lee, C. J.; Lee, M. S. SERS of Dithiocarbamate Pesticides Adsorbed on Silver Surface. *Bull. Korean Chem. Soc.* **2002**, *23*, 1604−1610.
(65) Grabar, K. C.; Freeman, R. G.; Hommer, M. B.; Natan, M. J. Preparation and Characterization of Au Colloid Monolayers. *Anal. Chem.* **1995**, *67*, 735−743.
(66) Haiss, W.; Thanh, N. T. K.; Aveard, J.; Fernig, D. G. Determination of Size and Concentration of Gold Nanoparticles from UV−vis Spectra. *Anal. Chem.* **2007**, *79*, 4215−4221.
(67) Zhang, Q.; Cobley, C. M.; Au, L.; McKiernan, M.; Schwartz, A.; Chen, J.; Wen, L.; Xia, Y. Production of Ag Nanocubes on a Scale of 0.1 g per Batch by Protecting the NaHS-Mediated Polyol Synthesis with Argon. *ACS Appl. Mater. Interfaces* **2009**, *1*, 2044−2048.
(68) Khlebtsov, B. N.; Panfilova, E. V.; Khanadeev, V. A.; Bibikova, O. A.; Terentyuk, G. S.; Ivanov, A.; Rumyantseva, V.; Shilov, I.; Ryabova, A.; Loshchenov, V. B.; Khlebtsov, N. G. Nanocomposites Containing Silica-Coated Gold-Silver Nanocages and Yb-2,4-Dimethoxyhematoporphyrin: Multifunctional Capability of IR-Luminescence Detection, Photosensitization, and Photothermolysis. *ACS Nano* **2011**, *5*, 7077−7089.
(69) Yuan, H.; Khoury, C. G.; Hwang, H.; Wilson, C. M.; Grant, G. A.; Vo-Dinh, T. Gold Nanostars: Surfactant-Free Synthesis, 3D Modelling, and Two-Photon Photoluminescence Imaging. *Nanotechnology* **2012**, *23*, No. 075102.
(70) Johnson, P. B.; Christy, R. W. Optical Constants of Noble Metals. *Phys. Rev. B* **1972**, *6*, 4370−4379.

DOI: 10.1021/acsami.5b01652
ACS Appl. Mater. Interfaces 2015, 7, 6518−6529